Evolution of ice crystal regions on the microscale based on *in situ* observations

Minghui Diao[1,2], Mark A. Zondlo[1,2]*, Andrew J. Heymsfield[3], Stuart P. Beaton,[4] and David C. Rogers[4]

Affiliations:

[1]Dept. of Civil and Environmental Engineering, Princeton University, New Jersey, 08544, USA;

[2]Ctr. for Mid-Infrared Technologies for Health and the Environment, Princeton University, New Jersey, 08544, USA;

[3]Mesoscale and Microscale Meteorology, National Center for Atmospheric Research, Colorado, 80307, USA;

[4]Earth Observing Laboratory, National Center for Atmospheric Research, Colorado, 80021, USA.

***Corresponding Author:**

Mark A. Zondlo

Assistant Professor

Department of Civil and Environmental Engineering

Center for Mid-Infrared Technologies for Health and Environment

E209A, Engineering Quad, Olden Street, Princeton University

Princeton, NJ, 08544

Ph: (609) 258-5037

Email: mzondlo@princeton.edu

Abstract:

Microphysical properties of cirrus clouds largely influence their atmospheric radiative forcing. However, uncertainties remain in simulating/parameterizing the evolution of ice crystals. These uncertainties require more analyses in the Lagrangian view, yet most *in situ* observations are in the Eulerian view. Here we demonstrate a new method to separate out five phases of ice crystal evolution, using the horizontal spatial relationships between ice supersaturated regions (ISSRs) and ice crystal regions (ICRs). Based on global *in situ* datasets, we show that the samples of clear-sky ISSRs, ice crystal formation/growth and evaporation/sedimentation are ~20%, 10% and 70% of the total ISSR + ICR samples, respectively. In addition, the variance of number-weighted mean diameter (Dc) becomes narrower during the evolution, while the distribution of ice crystal number density (Nc) becomes wider. The new method helps to understand the evolution of ICRs and ISSRs on the microscale by using *in situ* Eulerian observations.

1. Introduction

Cirrus clouds are ice clouds in the upper troposphere and have a large impact on the Earth's climate [*Chen et al.*, 2000]. In particular, the microphysical properties of cirrus clouds strongly influence cloud radiative forcing [*Fusina et al.*, 2007] and the efficiency of dehydration at the tropical tropopause layer [*Jensen et al.*, 2013]. Because the microphysical properties of cirrus clouds can be highly variable both temporally [*Barahona and Nenes*, 2011] and spatially [*Jensen et al.*, 2013], it is important to understand how these microphysical features evolve on a small scale. Recent cloud models have developed simulation schemes to address the time evolution of ice crystal properties, including the interactions between ice crystals and aerosols as well as the influences of micro- to mesoscale dynamic variabilities [*Jensen et al.*, 2010;

Barahona and Nenes, 2011]. In addition, recent climate models have also included new parameterizations of ice microphysical processes, such as ice nucleation under various aerosol loadings [*Hendricks et al.*, 2011; *Gettelman et al.*, 2012] and competitions between homogeneous and heterogeneous nucleation modes [*Spichtinger and Gierens*, 2009; *Liu et al.*, 2012].

With the new developments in cloud and climate models, it is critical to validate and constrain them with high resolution observations, especially since large uncertainties still remain in ice nucleation parameterizations [*Betancourt et al.*, 2012]. However, most *in situ* observations, such as aircraft-based and balloon-based observations, are not designed to follow the same air parcel, which means that these observations usually cannot be directly compared with Lagrangian model simulations. Previous lidar [*Comstock*, 2004; *Comstock et al.*, 2008] and aircraft observations [*Jensen*, 2005; *Jensen et al.*, 2008] were assumed to be contained within the same air parcel when compared with Lagrangian model simulations. Other studies used back trajectories coupled with aircraft observations to determine the relative humidity (RH) before and after ice crystal formation, respectively [*Gensch et al.*, 2008]. These previous analyses only provided a limited number of case studies which were restricted to certain meteorological backgrounds and geographical locations.

In order to directly compare with model simulations of ice microphysical evolution, a new analysis method is described here to analyze ice crystal evolution using aircraft-based *in situ* Eulerian observations. This method categorizes the extensive Eulerian sampling of ISSRs and ICRs into multiple evolution phases, including clear-sky ISS, nucleation, growth and sedimentation/evaporation.

2. Dataset and instrumentations

In this study we used the 1 Hz (~200 m) aircraft-based observations from the NSF Gulfstream-V (GV) research aircraft during the NSF Stratosphere Troposphere Analyses of Regional Transport 2008 (START08) campaign [*Pan et al.*, 2010]. START08 sampled the upper troposphere and lower stratosphere (UT/LS) over North America in April-June, 2008, providing ~90 transects across the thermal tropopause. All the samples were restricted to temperature ≤ -40°C (~6.1 to 14.9 km) to exclude the coexistence of supercooled liquid water droplets with ice crystals. Water vapor was measured by the 25 Hz, open-path Vertical Cavity Surface Emitting Laser (VCSEL) hygrometer [*Zondlo et al.*, 2010]. The water vapor measurements were averaged to 1 s for consistency with the temperature measurements. Temperature was recorded by a Rosemount temperature probe. The VCSEL hygrometer and the Rosemount probe have precisions of 1% and 0.01 K, respectively. Uncertainties in relative humidity with respect to ice (RHi) at 233–205 K were 8–10% after combining the uncertainties from the VCSEL hygrometer (6%) and temperature probe (± 0.5 K). The mean true air speed of the aircraft for current analyses was ~240 m/s.

Ice particles were sampled with the HIAPER Small Ice Detector Probe (SID-2H) instrument on the GV aircraft [*Cotton et al.*, 2010]. The trigger threshold diameter of SID-2H is 3 μm, and the measurement range is 1-50 μm. Ice crystal regions (ICRs) are defined as the locations where the total ice particle concentrations are greater than 0.06 #/cm^3 during the 1 Hz measurements, while the remaining regions are considered to be clear-sky regions. We used 0.06 #/cm^3 as the threshold for determining the presence of ice crystals because it represents a sampling rate greater than one particle per second at a sampling volume of 16 cm^3 each second. Above this range, the ice probe functions well for distinguishing between ice crystals and liquid

aerosols. The final dataset includes ~61 hr at T ≤ -40°C with ~2.3 hr and ~1.6 hr of ISS and ICR observations, respectively. The overlap between ISS and ICR is ~0.7 hr. The probability density function (PDF) of in-cloud RHi peaked at ~97%, which is consistent with previous observations [*Ovarlez et al.*, 2002; *Kahn et al.*, 2009].

3. Method

In this study, we use a new method to separate five evolution phases of ice crystals from Eulerian observations. The strength of this method is that it only requires two commonly-used parameters: 1) RHi and 2) presence or absence of ice crystals.

We define a set of spatially continuous ISSRs and ICRs (Figure 1, labeled as ISSR+ICR) as one sample. For example, if there are several ISSRs and ICRs intersecting each other, we consider the whole region containing all these ISSRs and ICRs as one sample. We calculate the fraction of ISSR+ICR with ice crystals (Figure 1 a, $M = \mathrm{sum}(L_{ICR}) / L_{ISSR+ICR}$) and the fraction of ISSR+ICR with ISS ($N = \mathrm{sum}(L_{ISSR}) / L_{ISSR+ICR}$). Here L denotes the length. M and N represent the horizontal fraction, since the aircraft horizontal true air speed is almost always at least ~20 times higher than the vertical speed. Because ISSRs and ICRs can overlap, these two fractions (M and N) are independent of each other and range between 0 and 1.

We use the combinations of M and N to define five phases of ice crystal evolution (Table 1). Phase 1 represents clear-sky ISSRs, i.e., no ice crystals exist inside the ISSR+ICR sample ($M = 0, N = 1$). In Phase 2, ISSRs start to have ice crystals inside ($0 < M < 1, N = 1$), which suggests that these ice crystals are newly formed because they haven't depleted all the water vapor over saturation yet. Therefore we name Phase 2 as the nucleation phase as it occurs very shortly after nucleation. Phase 3 is when the ISSR+ICR sample is no longer fully supersaturated, i.e., ISSRs

and ICRs are adjacent or they intersect each other. Phase 4 is when the whole sample has ice crystals and only part of it is still supersaturated ($M = 1$, $0 < N \leq 1$). We name Phase 3 and 4 as early and later growth phases, respectively. In Phase 5, ice crystals are in subsaturated conditions, which represent evaporation and sedimentation. The number of samples in each phase is shown in Table 1. To represent the expansion of ICRs with respect to ISSRs in the nucleation/growth phases, we define ratio $Q = \text{sum}(L_{ICR}) / \text{sum}(L_{ISSR})$. As ICRs enlarge in space and ISSRs become smaller, the Q value increases. For reference, Q is the same as the overlap ratio (i.e., the overlap length of ISSRs and ICRs versus the total length) when ICRs are buried inside ISSRs, and Q is also the inverse of the overlap ratio when ISSRs are buried inside ICRs.

4. Results

4.1 Evolution of RHi

To examine whether this method agrees with the theoretical ice crystal formation processes, we calculated the mean RHi value of each ISSR + ICR sample from Phase 1 to 5. The time evolution of Phase 1 to 4 is represented from left to right of the abscissa (Figures 2a and b), while Phase 5 is from right to left (Figure 2c).

For clear-sky ISSRs (Phase 1), no ice crystals exist and RHi is always above 100% (Figure 2a). As the horizontal extent of the ISSRs becomes larger, the mean RHi value also becomes larger, which agrees with the formation of ISSRs by large scale uplift [*Spichtinger et al.*, 2005], i.e., as ISSRs get uplifted and further cooled, ISS values increase and ISSRs expand. During ice crystal formation and growth (Phases 2, 3 and 4), ICRs gradually take over the space as they grow from smaller than ISSRs ($Q < 1$) to larger than ISSRs ($Q > 1$) (Figure 2b). The decreasing trend of mean RHi from supersaturation to subsaturation agrees with the depletion of

water vapor as ice crystals form, grow and sediment. Finally, ICRs get smaller as ice crystals evaporate and sediment in subsaturated conditions (Figure 2c). This feature agrees with previous simulations that ICRs become more scattered in the sedimentation stage [*Jensen*, 2005; *Fusina and Spichtinger*, 2010]. In addition, the range of RHi distributions in Phase 5 broadens as ICRs become smaller. The larger ICRs are closer to saturation while the smaller ICRs have RHi from ~5% to 100%. The wide range of RHi distribution results from the transport of ice crystals into much drier conditions. Overall, the observed RHi evolution agrees well with a previous cirrus cloud model study [*Fusina and Spichtinger*, 2010]. The simulation also shows the nucleation phase with ICRs buried inside ISSRs, the growth phase with decreasing RHi and expanding ICRs, and the sedimentation phase with wide RHi distributions from ~60% to 100%.

Combining all the phases together, we use the length of total ISSR+ICR regions as an indicator of time evolution (Figure 2d), i.e., expanding ISSR+ICR regions from Phases 1 to 4, and shrinking ICR regions for Phase 5. Although not shown here, the evolution of maximum RHi values inside the ISSR+ICR samples shows a similar trend as the evolution of mean RHi values. Figure 2d shows that the larger ISSR+ICR samples (> 10 km) are mostly in the nucleation and growth phases. We caution that the evolution indicator of ISSR+ICR length is not as precise as spatial ratio Q in Figure 2b, since there might be smaller ISSR+ICR regions with aged ice crystals and larger regions with newly formed ice crystals.

4.2 Evolution of ice crystal properties

With this new method, we analyze the evolution of ice crystal properties. Figures 3a and b show the evolution of ice crystal number density (Nc) (in logscale) and number-weighted mean diameter Dc (in μm) with respect to the spatial ratio Q of ICR/ISSR. We note that these Nc and

Dc analyses were restricted to the measurement dynamic size range of SID-2H instrument (1–50 μm). Here each marker of Nc and Dc in Figures 3a and b represent the mean Nc and Dc values for the ICR part in each sample, respectively. As ICRs gradually take over the space of ISSRs, both the mean Nc value and its standard deviation (1σ, shown as the error bar) of each ratio bin increase. The increasing Nc agrees with previous simulations, where new ice crystals continue to form with continuous uplifting [*Spichtinger and Gierens*, 2009]. On the other hand, not all ICRs experience the same process, which leads to the wide range of Nc distribution for aged ICRs.

Similar to Nc, the mean value of Dc in each ratio bin increases as ICRs evolve. However, in contrast to the increasing range of the Nc distribution, the range of the Dc distribution decreases with ice crystal growth, which agrees with the theoretical growth of ice crystals via water vapor diffusion [*Rogers and Yau*, 1989; *Straka*, 2009]. Both the growth rate of ice crystals and the RHi values decrease when the ice crystals become larger, and eventually the size distribution narrows as shown in Figure 3b.

Because Phase 5 cannot be shown in Figures 3a and 3b, we show the evolution of Nc and Dc with respect to the lengths of ICRs in Figures 3c and 3d, respectively. The Nc values decrease as the lengths of ICRs decrease, which agree with the previous simulation of *Spichtinger and Gierens* [2009] for the dissipation stage of cirrus clouds. The RHi color coding of Figures 3c and 3d show that most (~80%) small Dc below 10 μm happen at low RHi (< 60%), suggesting that sublimation plays an important role in decreasing ice crystal sizes in aged ICRs. Overall, the proportion of small ice crystals (Dc < 10 μm) in the nucleation phase (Phase 2), the early and later growth phases (Phases 3 and 4) and the sedimentation/evaporation phase are 21%, 0%, and 61%, respectively. These different Dc distributions in different phases show the importance of separating these phases for analyzing ice crystal evolution. The SID-2H

instrument is mostly immune to ice shattering [*Cotton et al.*, 2010], yet large ice particles beyond the SID-2H dynamic range (1–50 μm) were not included in these Dc and Nc analyses. Analyses of larger ice crystals are shown in supplementary Figure 2 using a different instrument and dataset. We note that the current method only requires the knowledge of the presence of ice crystals to separate five evolution phases, but the analyses of Nc and Dc could be complicated by ice shattering depending on the probes being used [*Field et al.*, 2006; *Cooper and Garrett*, 2010].

4.3 Lifetime ratio for five phases

Using the five phases of ice crystal evolution, we estimate the ratio of each phase within the whole evolution lifetime. Figure 4a shows the probability of Phases 1 to 5, normalized by the total number of ISSR+ICR samples. The clear-sky ISSRs (Phase 1), the coexisting ISSRs and ICRs (Phases 2 to 4) and the subsaturated ICRs (Phase 5) contribute to 20%, 10% and 70% of the total ISSR+ICR samples. The probability of each phase is an indicator of their temporal duration, which is also comparable to previous simulation results. For example, as shown in *Spichtinger and Gierens* [2009], during a 300 minute ice crystal evolution, the clear-sky ISSRs exist from 0-100 minutes (~30%), ice crystal diffusional growth consumes most ISSRs within 30 min (~10%) and ice crystals sediment from 130-300 min (~60%). The slight difference between the observations and the previous simulation are likely due to the sampling/modeling of different conditions.

Figure 4b shows the probability of each bin of spatial ratio Q with respect to the whole ISSR+ICR sampling. A large proportion (41%) of ICRs in nucleation and growth phases (Phases 2 to 4) happens when ISSRs and ICRs have similar spatial extents ($0.5 \leq Q < 2$). This feature indicates that for ISSRs with ice crystals, ICRs expand relatively fast to the extent of ISSRs,

which agrees with the previous simulation result that ice crystals appear throughout the whole depth of ISSRs almost simultaneously [*Spichtinger and Gierens,* 2009].

5. Implications for cloud modeling and ice nucleation studies

The method shown in this study only requires the measurement of RHi and the detection of ice crystals, which can be easily applied to most Eulerian observations, including both aircraft-based and ground-based observations. Different RHi values and ice crystal properties were shown at different evolution phases, which illustrate the importance of separating these phases for analyzing ice crystal evolution. To demonstrate the general applicability of our method, we also use a global dataset from the HIAPER Pole-to-Pole Observations (HIPPO) Global Campaign [*Wofsy et al.,* 2011] with the 2DC particle probe [*Korolev et al.*, 2011] (see supplementary material). The measurement range of 2DC probe is nominally 25–800 μm. Despite the different instrumentation and flight tracks, the overall trend of Nc and Dc evolution and the probability of the evolution phases shown by SID-2H (START08) and 2DC (HIPPO) probes are similar. For example, the clear-sky ISSRs, coexisting ISSRs and ICRs and subsaturated ICRs are 30%, 10% and 60% of the total samples in HIPPO campaign, respectively, which are comparable to the results of START08.

We caution that this method has several limitations. The method requires the observations of ISS in the nucleation phase, which means that ice crystals generated near saturation may be overlooked by this method. The vertical and horizontal transport of ice crystals are not discussed here with 1-D Eulerian sampling. Thus, the ice crystals falling from higher altitudes into lower ISSRs would be treated as newly-formed ice crystals even though they are not. In addition, the evolution here is in the view of the horizontal ISSR+ICR region instead of

the whole cirrus cloud, since a cirrus cloud may contain multiple phases at the same time. For example, the top layer of a cirrus cloud may be nucleating, while the lower levels may have ice crystals in growth and sedimentation. Another limitation of the method is that not all the cirrus clouds may experience all five phases. For example, an in-situ generated cirrus might experience the clear-sky ISSR phase until ice crystals form in the nucleation phase, but a convective-generated cirrus might already have ice crystals existing before RHi reaches 100% and therefore no clear-sky ISS is experienced.

Our method may be able to distinguish between individual homogeneous and heterogeneous freezing modes from different ISSR+ICR samples based upon their distinctive Nc and Dc values. For example, in Figure 3b, two different groups of Dc values have been observed above/below 10 μm, which may reflect different nucleation mechanisms. However, if the two freezing modes coexist in the same sample, the mean Nc and Dc values may not resolve the different populations of ice crystals.

Current work does not account for the absolute time duration in each phase because of the Eulerian sampling. Future studies are needed to combine both Lagrangian and Eulerian observations to determine the absolute time duration of each evolution phase. More modeling work is needed to conduct direct comparisons between the observed ice crystal evolution and Lagrangian simulations.

References

Barahona, D., and A. Nenes (2011), Dynamical states of low temperature cirrus, *Atmospheric Chemistry and Physics*, *11*(8), 3757–3771, doi:10.5194/acp-11-3757-2011.

Betancourt, R. M., D. Lee, L. Oreopoulos, Y. C. Sud, D. Barahona, and A. Nenes (2012), Sensitivity of cirrus and mixed-phase clouds to the ice nuclei spectra in McRAS-AC: single

column model simulations, *Atmos. Chem. Phys.*, *12*, 10679–10692, doi:10.5194/acp-12-10679-2012.

Chen, T., W. B. Rossow, and Y. Zhang (2000), Radiative Effects of Cloud-Type Variations, *Journal of Climate*, *13*(1), 264–286, doi:10.1175/1520-0442(2000)013<0264:REOCTV>2.0.CO;2.

Comstock, J. M. (2004), Ground-based lidar and radar remote sensing of tropical cirrus clouds at Nauru Island: Cloud statistics and radiative impacts, *Journal of Geophysical Research*, *107*(D23), 4714, doi:10.1029/2002JD002203.

Comstock, J. M., R.-F. Lin, D. O. Starr, and P. Yang (2008), Understanding ice supersaturation, particle growth, and number concentration in cirrus clouds, *Journal of Geophysical Research*, *113*(D23), D23211, doi:10.1029/2008JD010332.

Cooper, S. J., and T. J. Garrett (2010), Identification of Small Ice Cloud Particles Using Passive Radiometric Observations, *J. Appl. Meteor. Climatol.*, *49*, 2334–2347.

Cotton, R., S. Osborne, Z. Ulanowski, E. Hirst, P. H. Kaye, and R. S. Greenaway (2010), The Ability of the Small Ice Detector (SID-2) to Characterize Cloud Particle and Aerosol Morphologies Obtained during Flights of the FAAM BAe-146 Research Aircraft, *Journal of Atmospheric and Oceanic Technology*, *27*(2), 290–303, doi:10.1175/2009JTECHA1282.1.

Field, P. R., A. J. Heymsfield, and A. Bansemer (2006), Shattering and Particle Interarrival Times Measured by Optical Array Probes in Ice Clouds, *Journal of Atmospheric and Oceanic Technology*, *23*(10), 1357–1371, doi:10.1175/JTECH1922.1.

Fusina, F., and P. Spichtinger (2010), Cirrus clouds triggered by radiation, a multiscale phenomenon, *Atmospheric Chemistry and Physics*, *10*(11), 5179–5190, doi:10.5194/acp-10-5179-2010.

Fusina, F., P. Spichtinger, and U. Lohmann (2007), Impact of ice supersaturated regions and thin cirrus on radiation in the midlatitudes, *Journal of Geophysical Research*, *112*(December), D24S14, doi:10.1029/2007JD008449.

Gensch, I. V et al. (2008), Supersaturations, microphysics and nitric acid partitioning in a cold cirrus cloud observed during CR-AVE 2006: an observation–modelling intercomparison study, *Environmental Research Letters*, *3*(3), 035003, doi:10.1088/1748-9326/3/3/035003.

Gettelman, A., X. Liu, D. Barahona, U. Lohmann, and C. Chen (2012), Climate impacts of ice nucleation, *Journal of Geophysical Research*, *117*(D20), D20201, doi:10.1029/2012JD017950.

Hendricks, J., B. Kärcher, and U. Lohmann (2011), Effects of ice nuclei on cirrus clouds in a global climate model, *Journal of Geophysical Research*, *116*(D18206), 1–24.

279 Jensen, E. J. (2005), Formation of a tropopause cirrus layer observed over Florida during
280 CRYSTAL-FACE, *Journal of Geophysical Research*, *110*(D3), D03208,
281 doi:10.1029/2004JD004671.

282 Jensen, E. J. et al. (2008), Formation of large (≈100 μm) ice crystals near the tropical tropopause,
283 *Atmospheric Chemistry and Physics*, *8*(6), 1621–1633, doi:10.5194/acp-8-1621-2008.

284 Jensen, E. J., L. Pfister, T.-P. Bui, P. Lawson, and D. Baumgardner (2010), Ice nucleation and
285 cloud microphysical properties in tropical tropopause layer cirrus, *Atmospheric Chemistry*
286 *and Physics*, *10*(3), 1369–1384, doi:10.5194/acp-10-1369-2010.

287 Jensen, E. J., G. Diskin, R. P. Lawson, S. Lance, T. P. Bui, D. Hlavka, M. McGill, L. Pfister, O.
288 B. Toon, and R. Gao (2013), Ice nucleation and dehydration in the Tropical Tropopause
289 Layer., *Proceedings of the National Academy of Sciences of the United States of America*,
290 1217104110, doi:10.1073/pnas.1217104110.

291 Kahn, B. H., A. Gettelman, E. J. Fetzer, A. Eldering, and C. K. Liang (2009), Cloudy and clear-
292 sky relative humidity in the upper troposphere observed by the A-train, *Journal of*
293 *Geophysical Research*, *114*(D4), D00H02, doi:10.1029/2009JD011738.

294 Korolev, A. V., E. F. Emery, J. W. Strapp, S. G. Cober, G. A. Isaac, M. Wasey, and D. Marcotte
295 (2011), Small Ice Particles in Tropospheric Clouds: Fact or Artifact? Airborne Icing
296 Instrumentation Evaluation Experiment, *Bulletin of the American Meteorological Society*,
297 *92*(8), 967–973, doi:10.1175/2010BAMS3141.1.

298 Liu, X., X. Shi, K. Zhang, E. J. Jensen, A. Gettelman, D. Barahona, A. Nenes, and P. Lawson
299 (2012), Sensitivity studies of dust ice nuclei effect on cirrus clouds with the Community
300 Atmosphere Model CAM5, *Atmospheric Chemistry and Physics*, *12*(24), 12061–12079,
301 doi:10.5194/acp-12-12061-2012.

302 Ovarlez, J., J. F. Gayet, K. Gierens, J. Strom, H. Ovarlez, F. Auriol, R. Busen, and U. Schumann
303 (2002), Water vapour measurements inside cirrus clouds in Northern and Southern
304 hemispheres during INCA, *Geophysical Research Letters*, *29*(16), 1813.

305 Pan, L. L. et al. (2010), The Stratosphere–Troposphere Analyses of Regional Transport 2008
306 Experiment, *Bulletin of the American Meteorological Society*, *91*(3), 327–342,
307 doi:10.1175/2009BAMS2865.1.

308 Rogers, R. R., and M. K. Yau (1989), *A short course in cloud physics*, Pergamon Press.

309 Spichtinger, P., and K. M. Gierens (2009), Modelling of cirrus clouds – Part 2 : Competition of
310 different nucleation mechanisms, *Atmospheric Chemistry & Physics*, *9*, 2319–2334.

311 Spichtinger, P., K. Gierens, and H. Wernli (2005), A case study on the formation and evolution
312 of ice supersaturation in the vicinity of a warm conveyor belt's outflow region, *Atmospheric*
313 *Chemistry & Physics*, *5*, 973–987.

Straka, J. M. (2009), *Cloud and precipitation microphysics - principles and parameterizations*, 1st ed., Cambridge University Press.

Wofsy, S. C. et al. (2011), HIAPER Pole-to-Pole Observations (HIPPO): fine-grained, global-scale measurements of climatically important atmospheric gases and aerosols., *Philosophical transactions. Series A, Mathematical, physical, and engineering sciences*, *369*(1943), 2073–86, doi:10.1098/rsta.2010.0313.

Zondlo, M. A., M. E. Paige, S. M. Massick, and J. A. Silver (2010), Vertical cavity laser hygrometer for the National Science Foundation Gulfstream-V aircraft, *Journal of Geophysical Research*, *115*(D20), D20309, doi:10.1029/2010JD014445.

Acknowledgement

We gratefully acknowledge funding for field support and data analyses from the following sources: NSF ATM-0840732 for VCSEL (Princeton). M.D. gratefully acknowledges support from the NASA Earth and Space Science Graduate Fellowship, NASA NNX09AO51H. We appreciate the efforts of NCAR EOL flight, technical, and mechanical crews during START08 campaign, in particular, P. Romashkin for field maintenance of the VCSEL hygrometer. We also appreciate helpful discussions with L. Donner, S. Fueglistaler and L. L. Pan.

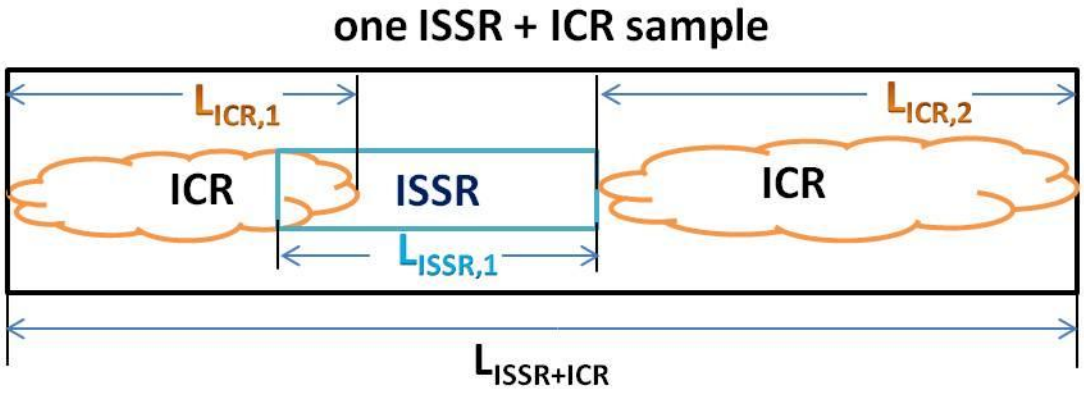

Figure 1. Spatial ratios of ISSRs and ICRs inside one ISSR+ICR sample. Here L_{ICR} and L_{ISSR} represent the 1-D horizontal extents of ICRs and ISSRs inside the ISSR+ICR sample, respectively. $L_{ISSR+ICR}$ represents the whole ISSR+ICR extent.

337 Table 1. Definitions of five phases based on the combinations of M and N.

Phase	**Description**	**Spatial ratio M = sum(L_{ICR}) / $L_{ISSR+ICR}$**	**Spatial ratio N = sum(L_{ISSR}) / $L_{ISSR+ICR}$**	**Number of samples (ISSR + ICR)**
1	Clear-sky ISSRs	0	1	237
2	Nucleation	$0 < M < 1$	1	34
3	Early growth of ice crystals	$0 < M < 1$	$0 < N < 1$	55
4	Later growth of ice crystals	1	$0 < N \leq 1$	23
5	Sedimentation/evaporation	1	0	815

338

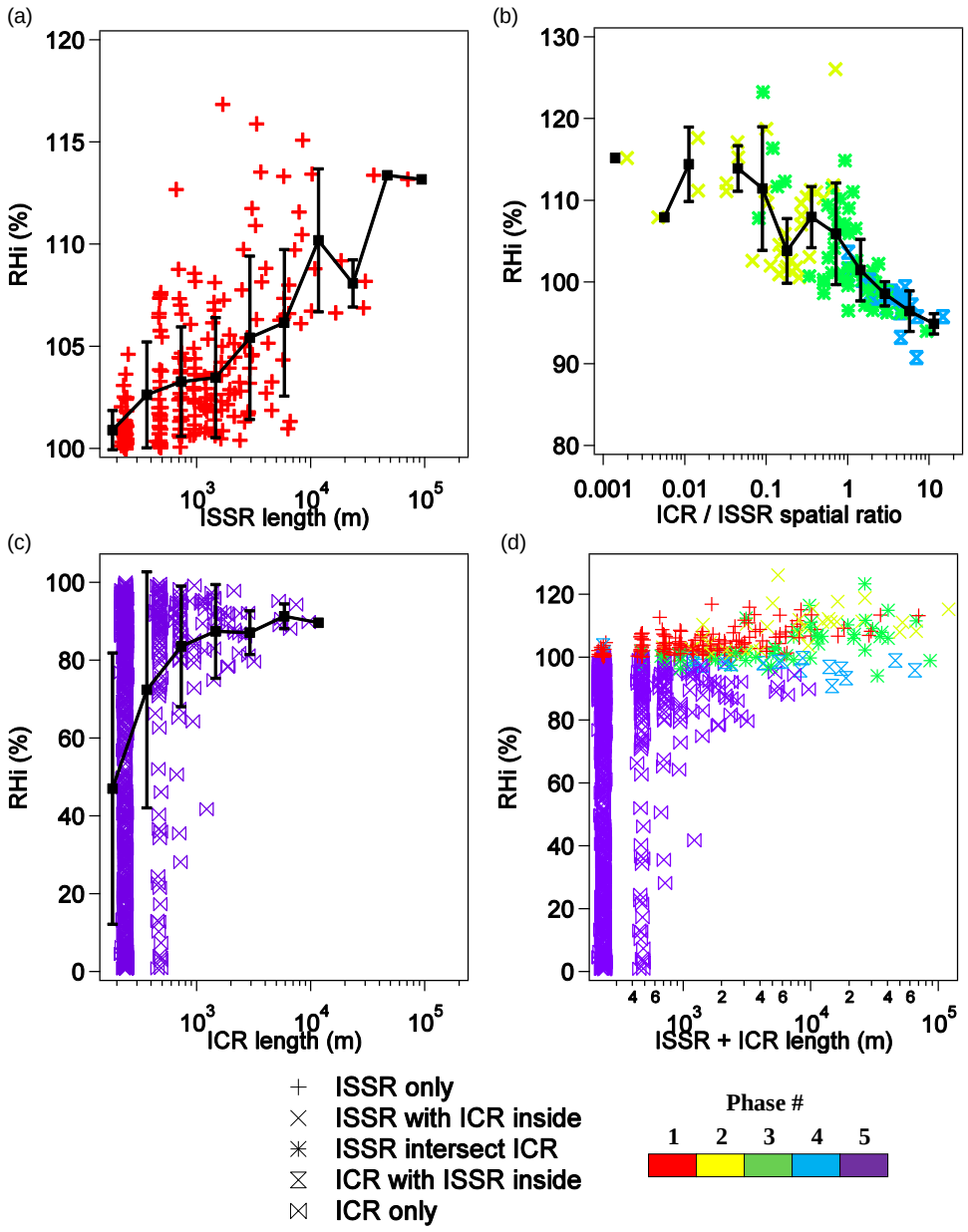

339

340 **Figure 2**. RHi evolution for five evolution phases. (a) Phase 1 of clear-sky ISSRs; (b) Phases 2,
341 3 and 4 of ice crystal nucleation and growth; (c) Phase 5 of ice crystals in sedimentation/
342 evaporation; (d) All five phases. All binning of length scale and spatial ratios used 2^i to 2^{i+1} bins
343 (i = 1, 2 ,3…), centered at $2^{i+0.5}$. All error bars in this study show ± one standard deviation.

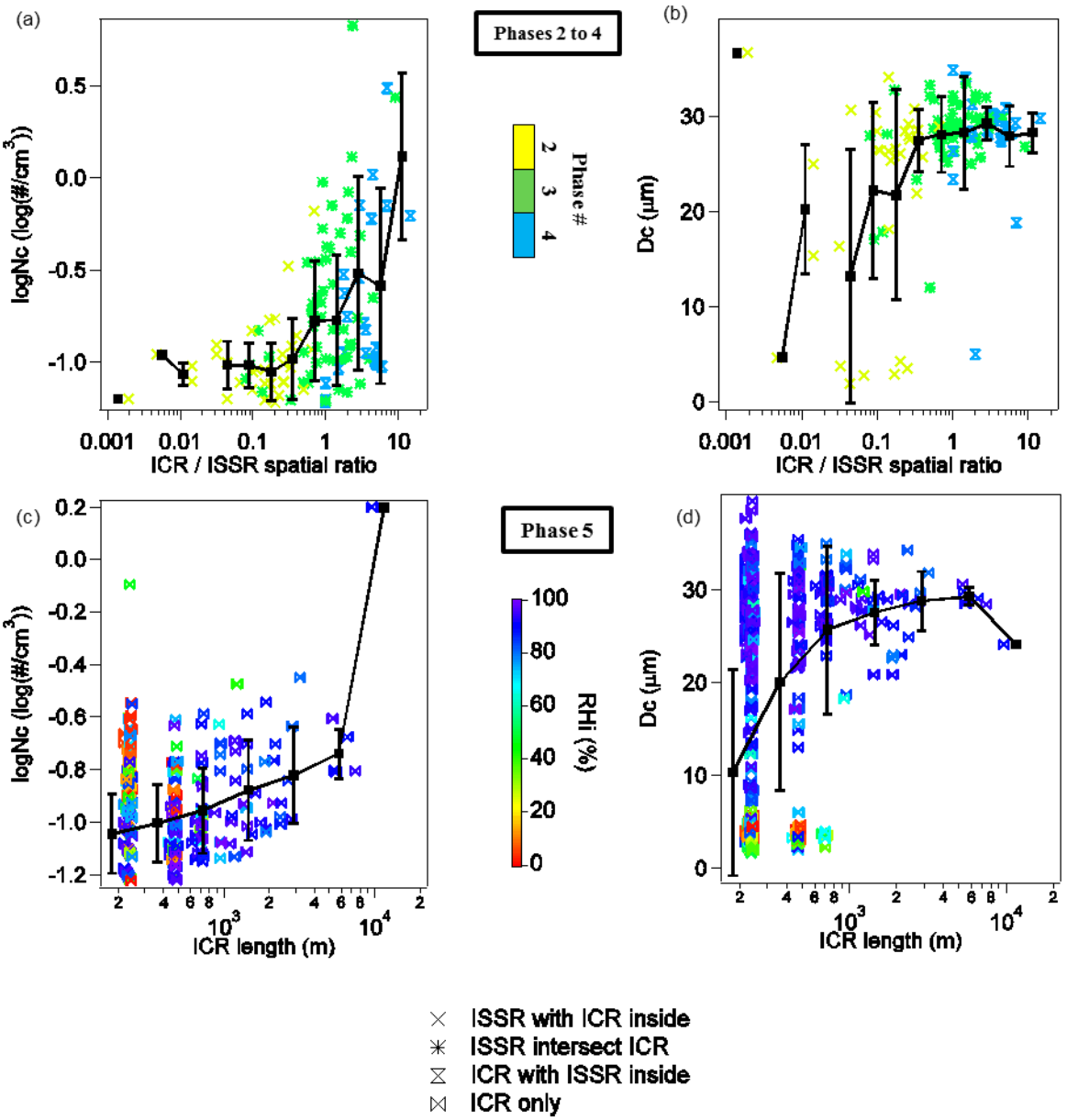

344

345 **Figure 3**. Evolution of ice crystal number density (Nc) and mean diameter (Dc). The evolution
346 of Nc and Dc in Phases 2 to 4 are shown in (a) and (b), respectively, colorcoded by the phase
347 number. The evolution of Nc and Dc in Phase 5 are shown in (c) and (d), respectively,
348 colorcoded by the mean RHi value. We note that Figures 3c and 3d used a different color code
349 than Figures 3a and 3b. The marker shape is the same as Figure 2.

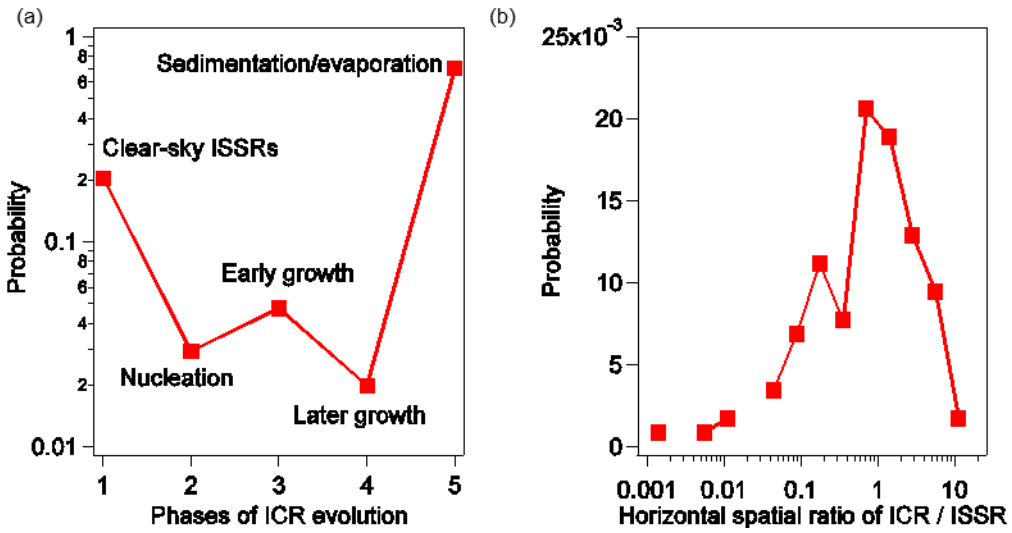

350

351 **Figure 4**. Probability of ice crystal evolution phases. (a) Probability of Phases 1 to 5, normalized
352 by total sample number of 1164. (b) Probability for each bin of spatial ratio Q (Q = ICR/ISSR),
353 also normalized by 1164.

The author has requested enhancement of the downloaded file. All in-text references underlined in blue are linked to publications on ResearchGate.